Inorganic Chemistry

pubs.acs.org/IC
Article

Observation of a Polar Compound with Halide Ordering in the Compositional Series $(CH_3NH_3)_2Te(Br_xCl_{1-x})_6$

Yuhan Liu, Prajna Bhatt, Roxy Lee, Avishek Dey, Anna Regoutz, Robin S. Perry, and Robert G. Palgrave*

Cite This: *Inorg. Chem.* 2025, 64, 21479−21488
Read Online

ACCESS | Metrics & More | Article Recommendations | Supporting Information

ABSTRACT: Single-crystal samples of compounds in the series $(CH_3NH_3)_2Te(Cl_{1-x}Br_x)_6$ were produced with counter-diffusion crystal growth in silica gels, and new crystal structures are determined using single-crystal X-ray diffraction. With increasing Br content, the structure transitions from $P\bar{3}m1$ to $P6_3mc$ to $R\bar{3}m$ and finally to $Fm\bar{3}m$. The compound with x≈0.068 adopts the polar $P6_3mc$ space group, and the structure has partially ordered Cl^- and Br^- ions. The crystals of this compound show distinct piezoelectric domains with different responses by Piezoresponse Force Microscopy (PFM), confirming their polar structure.

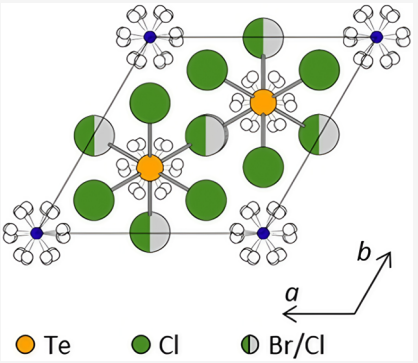

INTRODUCTION

Complex halide materials, containing halide anions and at least two different cations, as exemplified by halide perovskites, have proven to be extremely interesting and valuable materials undergoing renewed interest in recent years. Polar complex halides, like their well-studied oxide counterparts, may exhibit additional important properties such as piezoelectricity, ferroelectricity, effective charge separation, and high ionic conductivity, driven by their noncentrosymmetric crystal structures.[1] The synthesis of polar halide compounds with these properties may impact the current uses of complex halides in photovoltaics and optoelectronic materials or may enable new functionalities. Although the vast majority of halide perovskite and related compounds adopt centrosymmetric structures, some strategies have emerged to engineer noncentrosymmetric complex halide compounds.

The use of polar molecular cations at the A-site is a versatile method to introduce polar properties into complex halides.[2] Chiral halide perovskites can be produced using chiral molecular ions, which have been extensively studied.[3] At low temperatures, $CsSnBr_3$ has been found to crystallize in a polar space group driven by the asymmetry of the Sn(II) lone-pair cation.[4,5] $CsGeBr_3$ is also polar for similar reasons, and $ACuCl_4$ compounds, where A is a chlorinated organic molecular ion, are polar due to the orientation of the molecular ions.[6,7]

Anion ordering is another promising route for the formation of polar structures. Charles et al. studied anion ordering in oxyfluoride double perovskites $(A_2BMO_xF_{6-x})$.[8] There it was found that structural distortions, such as octahedral rotations, could couple with anion order to produce a large variety of nonpolar, polar, and chiral-polar structures. Anion order among halide (rather than oxy-halide) materials appears to be rare. Mixed bromide−iodide two−dimensional (2D) lead Ruddlesden−Popper phases were shown to display anion ordering, with Br appearing in the apical sites and I in the bridging sites of the 2D Pb halide layer.[9] In the triple perovskite $A_3B_2X_9$ series, bromide and iodide ordering has again been observed, which is driven by differences in the bridging and apical anion positions.[10] Due to the symmetrical nature of the Br−I ordering in both these cases, neither structure was found to be polar.

Another important complex halide family of compounds is the vacancy-ordered double perovskites with chemical formula A_2BX_6.[11−14] The A_2BX_6 family is characterized by isolated $[BX_6]^{2-}$ octahedra and is very commonly found in the $Fm\bar{3}m$ aristotype structure.[15] Lower symmetry structures result from distortions of the aristotype through correlative rotations of the $[BX_6]^{2-}$ octahedra and distortion of the cubic lattice, but some other A_2BX_6 structures are not subgroups of the cubic parent.[16] Hybrid A_2BX_6 compounds are those with molecular ion A-site cations, and add another layer of structural complexity.[17−20] The crystal structures of different hybrid A_2BX_6 compounds with organic cations were previously reported, and many of them undergo a structural phase transition at various temperatures.[21−23]

Received: July 22, 2025
Revised: September 25, 2025
Accepted: October 3, 2025
Published: October 22, 2025

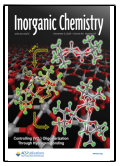

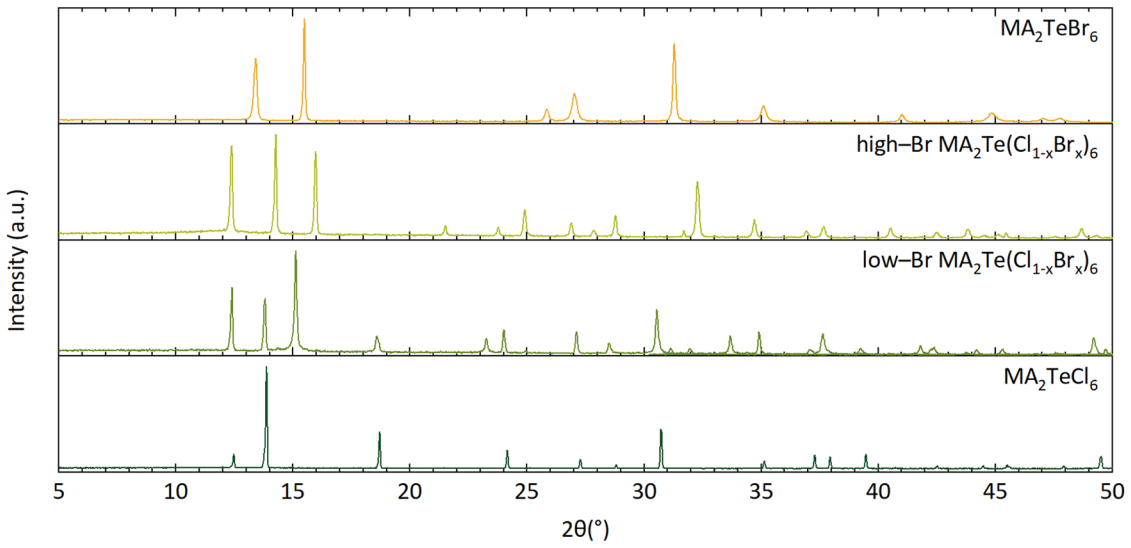

Figure 1. PXD patterns of the room-temperature $MA_2Te(Cl_{1-x}Br_x)_6$ phases (λ = 1.5406 Å).

In a previous work, we reported the phase transitions of MA_2TeCl_6 (MA = $CH_3NH_3^+$) at variable temperatures.[22] Here, we study the crystal structures of the $MA_2Te(Cl_{1-x}Br_x)_6$ series at room temperature. We demonstrate that careful control of the anion ratio leads to the formation of a polar structure containing partially ordered halide anions that is stable only in a narrow compositional range. We believe that this is the first report of a polar compound in which the polarity exists by virtue of halide ordering. This observation illustrates how the delicate balance between the ion sizes in A_2BX_6 compounds can lead to diverse physical properties.

EXPERIMENTAL SECTION

Single-Crystal Growth. The synthesis of $MA_2Te(Cl_{1-x}Br_x)_6$ was first attempted using solution-based coprecipitation and solid-state synthesis in a sealed ampule. However, neither approach resulted in a pure phase for low-Br $MA_2Te(Cl_{1-x}Br_x)_6$ (see SI).

Instead, $MA_2Te(Cl_{1-x}Br_x)_6$ single crystals were synthesized using the counter-diffusion crystal growth (CDCG) method in a silica hydrogel. $TeCl_4$ solution was first prepared by adding TeO_2 (Sigma-Aldrich, 99%) powder to 37 wt % HCl (Sigma-Aldrich). The solution was stirred for 1 h at 100 °C. Then, $TeBr_4$ powder (Alfa Aesar, 99.9%) was added to the cooled $TeCl_4$ solution based on the required stoichiometry to obtain a TeX_4 (X = Br, Cl) solution with the desired Br/Cl ratio. Finally, 2 mL of a 0.6 M aqueous solution of Na_2SiO_3 (Sigma-Aldrich) was added dropwise to the TeX_4 solution (~10 mL) under stirring. The beaker was then covered with parafilm and placed in a low-temperature oven at 29 °C for 48 h to form a TeX_4 silica gel.[24,25]

Methylamine solution (Sigma-Aldrich, 40 wt % in H_2O) was reacted with 37 wt % HCl (Sigma-Aldrich) at room temperature, and the resulting solution was stirred at 110 °C to precipitate MACl powder. After filtering and washing with diethyl ether (Fisher Chemical, 99.5%), the MACl precipitate was dried at 60 °C to produce a white powder. The MACl powder was then redissolved in DI water to form a saturated solution, which was carefully layered atop the previously prepared TeX_4 containing silica gel surface. Crystal formation was be observed through the gel, occurring between 4 and 7 days. All crystals were picked out using tweezers and dried overnight on filter paper in air. The CDCG method was conducted multiple times to ensure the reproducibility of the synthesis method with nominal 7 and 13% Br for the low-Br and high-Br compounds, respectively. The rationale for these concentrations are discussed in the Supporting Information.

DFT Calculations. Density functional theory (DFT) calculations were performed within periodic boundary conditions via the Vienna *Ab initio* Simulation Package (VASP).[26] The projector-augmented wave (PAW) method was used to describe the interaction between the core and valence electrons.[27,28] A version of the Perdew–Burke–Ernzehof (PBE)[29] functional that is adapted toward the description of solid state systems, PBEsol,[30] was used in this work. A Γ-centered 3 × 3 x 3 *k*-point mesh and a plane-wave cutoff energy of 350 eV were found to converge the total energy of all structures to within 1 meV per atom. The plane-wave cutoff energy was increased to 455 eV for geometry optimization calculations to avoid the possibility of Pulay stress.[31]

The Raman spectra were simulated using the methodology of Porezag et al.[32] To calculate the off-resonance Raman activity of a mode, the derivative of the polarizability with respect to the normal mode coordinate was computed using phonons at the Γ-point and macroscopic dielectric tensor from density functional perturbation theory (DFPT). The structures were relaxed with a tight ionic force criterion of 1×10^{-5} eV A^{-1} to increase the accuracy when calculating atomic forces and phonon frequencies. For the DFPT calculations, convergence with respect to the *k*-point density and plane-wave energy cutoff was confirmed for the ionic contribution to the static dielectric constant, $\in_{ionic}$. The off-resonance Raman activities were evaluated using the vasp_raman.py code.[33] To simulate the experimental line shape, Gaussian (2.0 eV) and Lorentzian (4.0 eV) broadening were applied to the simulated Raman spectra using the Galore software package.[34] The choice of alloy structures for calculated Raman spectra was previously determined by Karim et al. and is applied here as well.[35]

Characterization. Powder X-ray diffraction (PXD) was performed using a Stoe Stadi-P X-ray diffractometer with a Cu $K\alpha_1$ radiation source (λ = 1.5406 Å, 40 kV, 30 mA) in transmission mode. Data were collected from 5 to 50° at 0.5° per step for 15 s.

Single-crystal X-ray diffraction (SXD) was performed on an Agilent SuperNova diffractometer at 295 K. Data were collected with a Mo $K\alpha$ X-ray source (λ = 0.7107 Å) and processed with CrysAlisPro,[36] full spheres of data were collected to 0.8 Å resolution using 1° scan frames in ω. The crystal structure was solved using SHELXT and refined with SHELXL within the Olex2 software suite.[37−39] The refinement procedure forthe MA^+ cation was adapted from previous work.[22] Average bond angles, bond lengths, and projection distances between the halide and Te layers were calculated using Mercury[40] from the atomic coordinates derived from the SXD results. Bond angle variance and pseudocubic lattice parameters are calculated by VESTA.[41]

https://doi.org/10.1021/acs.inorgchem.5c03380
Inorg. Chem. 2025, 64, 21479−21488

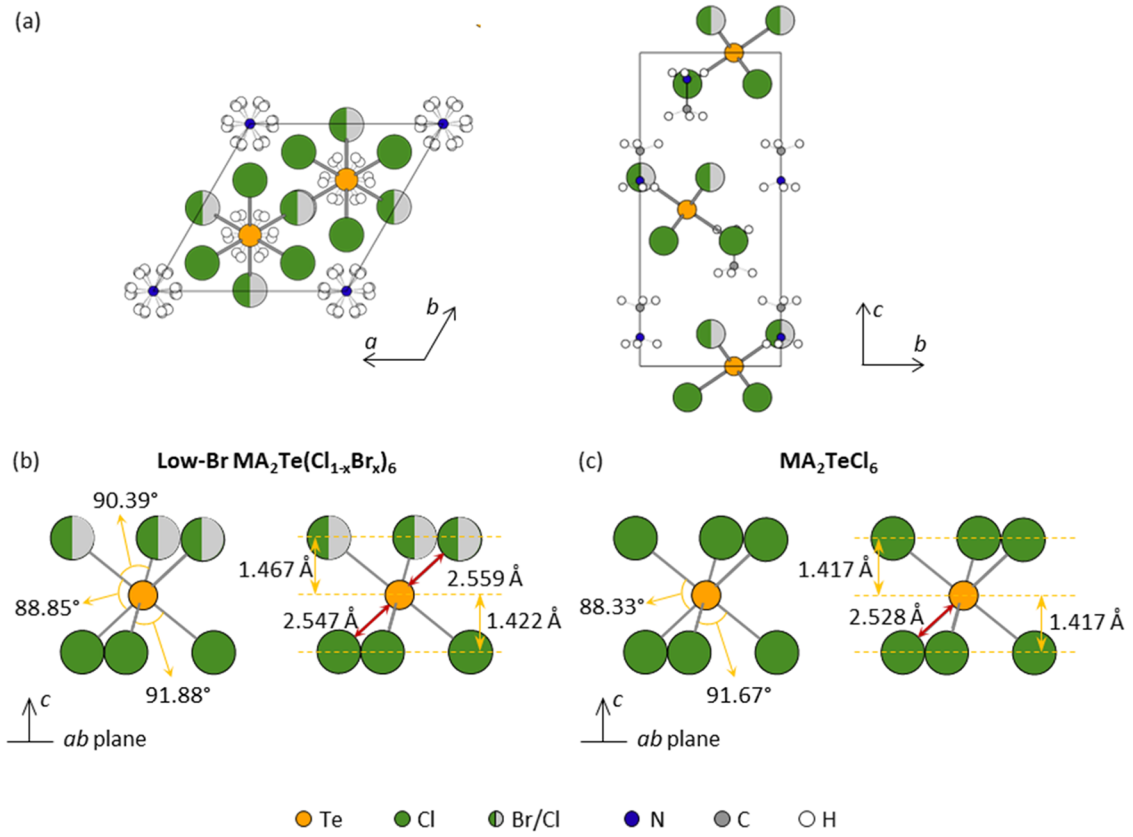

Figure 2. (a) Crystal structure of low-Br $MA_2Te(Cl_{1-x}Br_x)_6$ at 295 K, viewed along the *c*-axis (left) and down the *a*-axis (right). Schematic diagram of the $[TeX_6]^{2-}$ octahedra in (b) low-Br $MA_2Te(Cl_{1-x}Br_x)_6$ and (c) MA_2TeCl_6 in comparison. The values for MA_2TeCl_6 are obtained from previous work.[22] The yellow, green, light gray, blue, dark gray, and white circles represent Te, Cl, Br, N, C, and H atoms, respectively.

Raman spectra were obtained using a Renishaw 633 nm Raman spectrometer with a 50× objective lens. The spectral resolution was 4 cm^{-1} with a step size of 0.5 cm^{-1}.

X-ray photoelectron spectroscopy (XPS) was performed using a Thermo Scientific Kα spectrometer, which uses a monochromatized Al K_α X-ray source ($h\nu$ = 1486.6 eV), a hemispherical analyzer, and a two-dimensional detector. The electron energy analyzer consists of a double focusing 180° hemisphere with a mean radius of 125 mm, operated in constant analyzer energy (CAE) mode, and a 128-channel position sensitive detector. Measurements were conducted with a 400 μm spot size using a dual-beam flood gun (electron and Ar^+ ion) with a 100 mA current. The pass energy was 200 eV for the survey spectra and 40 eV for the core levels. The Thermo Avantage v5.9925 software package was used for XPS spectral analysis, and all spectral fittings were performed with a Shirley background.

Piezoresponse force microscopy (PFM) was carried out using a Bruker Dimension Icon atomic force microscope. To detect any piezoresponse in the crystals, an AC voltage with an amplitude of 3 V peak-to-peak near the contact resonance frequency was applied to the samples. The crystals were stuck to the AFM stage using conductive carbon tape. Bruker SCM-PIT-V2 silicon AFM probes with a Pt/Ir conductive coating and a nominal stiffness of 3 N m^{-1} were used for the measurements.

RESULTS AND DISCUSSION

Four distinct room-temperature structures were found in the series $MA_2Te(Cl_{1-x}Br_x)_6$ ($0 \le x \le 1$), including the known structures of the end members (x = 0,1), as shown in Figure S1. The PXD patterns of crushed CDCG single crystals are shown in Figure 1, and clearly indicate the different crystal structures of the two mixed-halide $MA_2Te(Cl_{1-x}Br_x)_6$ samples (labeled as low-Br and high-Br), in comparison to MA_2TeCl_6 (trigonal, $P\bar{3}m1$) or MA_2TeBr_6 (cubic, $Fm\bar{3}m$).[22,42] X-ray photoelectron spectroscopy (XPS) shows that the low-Br sample contains about 6.8% Br, while the high-Br sample contains 10.1% Br (see Table S2 and Figure S1). A similar composition-driven structural transition for organic hexaiodoplatinates, A_2PtI_6, has been previously reported.[43] SXD was then performed to examine the crystal structures of the two new phases.

Crystal Structures of MA_2TeCl_6 and MA_2TeBr_6. The structures of MA_2TeCl_6 and MA_2TeBr_6 have been previously reported, and we summarize the main features here to aid in the discussion of the new compounds.[22,44]

MA_2TeBr_6 crystallizes in the $Fm\bar{3}m$ space group, with lattice parameter a = 11.445(8) Å, a regular octahedral environment around Te, and a uniform Te−Br bond distance of 2.712(2) Å. The cell volume per formula unit is 374.8 $Å^3$. We consider this the aristotype structure from which most of the other structures discussed below can be derived by the distortion and rotation of the octahedra.

MA_2TeCl_6 crystallizes in the $P\bar{3}m1$ space group, a subgroup of $Fm\bar{3}m$, which can be reached by a rotation of the $[TeCl_6]^{2-}$ octahedra around each cubic axis, in this case by around 5.3°, and a slight distortion of the Te ions away from their positions in the cubic lattice. The octahedra themselves are almost undistorted with all Te−Cl bonds measuring2.528(1) Å and a bond angle variance of 2.37 deg^2.

Crystal Structure of Low-Br $MA_2Te(Cl_{1-x}Br_x)_6$. Single-crystal X-ray diffraction was carried out at 295 K on a low-Br $MA_2Te(Cl_{1-x}Br_x)_6$ sample. The space group was determined to be $P6_3mc$, and the cell volume per formula unit was 335.3

https://doi.org/10.1021/acs.inorgchem.5c03380
Inorg. Chem. 2025, 64, 21479−21488

Table 1. Projected Bond Lengths (e.g., Cl−Cl) and Intermolecular Distances (e.g., Cl···Cl) Calculated Using Mercury[40a]

	Along the *a*-axis		Along the *c*-axis			
MA_2TeCl_6 $P\bar{3}m1$	**Cl···Cl**	**Cl−Cl**	**Cl···Cl**	**Cl−Cl**	**N···Cl**	**C−N**
	3.730 Å	3.627 Å	4.248 Å	2.833 Å	0.136 Å	1.407 Å
Low-Br $P6_3mc$	**X(1)···X(1)**	**X(1)−X(1)**	**X(1)···X(2)**	**X(1)−X(2)**	**N(1)···X(1)**	**C(1)−N(1)**
	3.765 Å	3.632 Å	4.241 Å	2.889 Å	0.153 Å	1.356 Å
	X(2)···X(2)	**X(2)−X(2)**			**N(2)···X(2)**	**C(2)−N(2)**
	3.735 Å	3.661 Å			0.217 Å	1.359 Å
High-Br $R\bar{3}m$	**X···X**	**X−X**	**X···X**	**X−X**	**N···X**	**C−N**
	3.760 Å	3.673 Å	4.220 Å	2.942 Å	0.252 Å	1.394 Å

[a]The values for MA_2TeCl_6 are obtained from previous work.[22] Given that the typical error of the measured lattice parameters is less than 0.002 Å, the error for all of the projected distances and bond lengths is less than 0.002 Å.

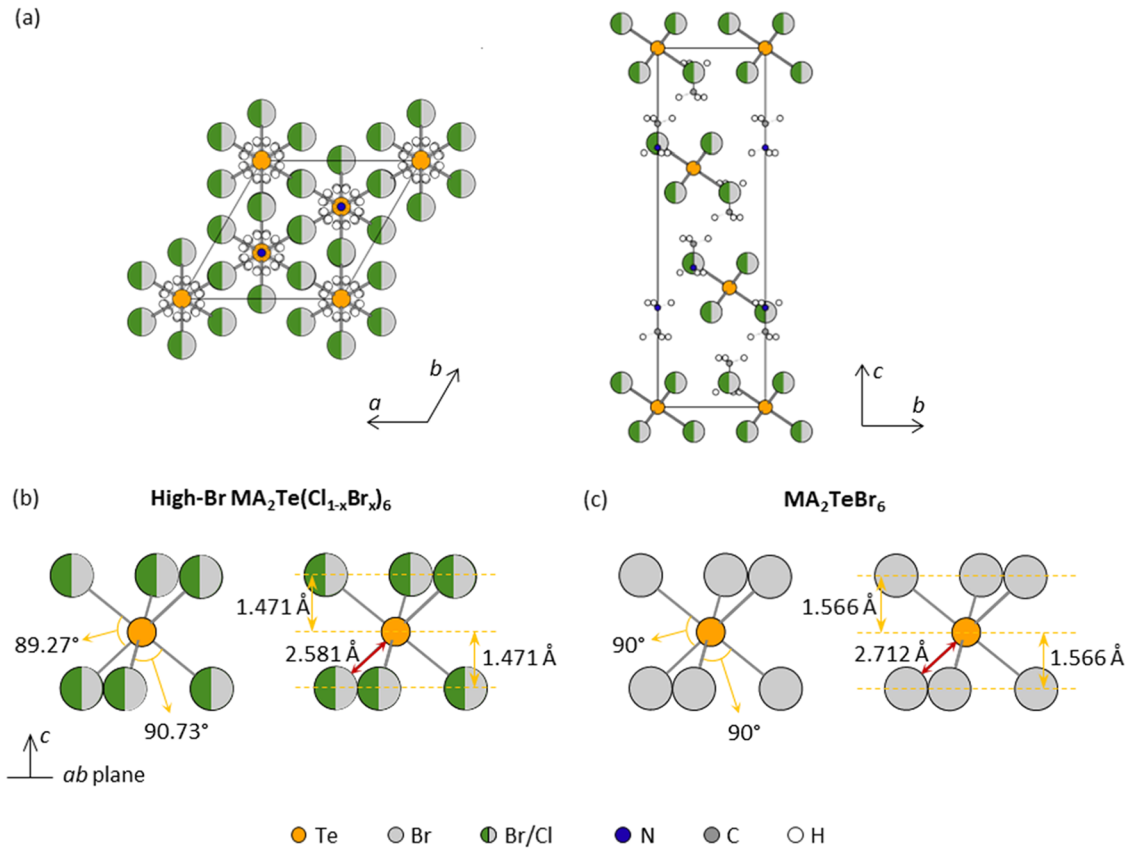

Figure 3. (a) Crystal structure of high-Br $MA_2Te(Cl_{1-x}Br_x)_6$ at 295 K, viewed along the *c*-axis (left) and down the *a*-axis (right). Schematic diagram of the $[TeX_6]^{2-}$ octahedra in (b) high-Br $MA_2Te(Cl_{1-x}Br_x)_6$ and (c) MA_2TeBr_6 in comparison. Yellow, green, light gray, blue, dark gray, and white circles represent Te, Cl, Br, N, C, and H atoms, respectively.

Å^3. As expected, this is larger than that in MA_2TeCl_6 due to the inclusion of some Br ions. The lattice parameter *a* increases to 7.3962(4) Å with the addition of Br, while *c* is doubled to 14.2588(14) Å, $Z = 2$ ($a = 7.3565(4)$ Å and $c = 7.0812(7)$ Å for MA_2TeCl_6).[6] As illustrated in Figure 2(a), the structure follows the $[TeX_6]^{2-}$−MA^+−MA^+−$[TeX_6]^{2-}$ stacking sequence as MA_2TeCl_6 along the *c*-axis, and MA^+ cations are still arranged parallel to the *c*-axis between octahedra. The $[TeX_6]^{2-}$ octahedra layer at $z = 1/2$ is separated from the layer at $z = 0$ by 2/3 and 1/3, respectively. For comparison, the octahedra in pure MA_2TeCl_6 are directly above each other along the *c*-axis.

The $P6_3mc$ space group of the low-Br crystal is not a subgroup of $Fm\bar{3}m$ and cannot be reached from the cubic aristotype by distortion or rotation of the octahedra. The bromide ions were found to partially occupy three positions in each $[TeX_6]^{2-}$ octahedron (the X(1) site), which appeared equivalent to those obtained by SXD, indicating that their long-range average composition was the same. The remaining three positions are occupied only by chloride ions (X(2) site). The X(1) and X(2) positions thus form separate alternating layers parallel to the *ab* plane. Refinement shows 8.6% Br occupancy on the X(1) site, with no Br on the X(2) site.

This leads to the distortion of the octahedra, as depicted in Figure 2(b). Two Te−X distances are observed, and the Te−X(1) distance (2.559(3) Å) is slightly longer than the Te−X(2) distance (2.547(3) Å), as Br^- (1.96 Å) has a larger ionic radius than Cl^- (1.81 Å).[45] The X(1)−Te−X(1) bond angle (90.39°) is smaller than the X(2)−Te−X(2) angle (91.88°). Consequently, the Te atom is not found equidistant between the X(1) and X(2) layers but is further away from the X(1) layer (1.467 Å) and closer to the X(2) layer (1.422 Å). The

https://doi.org/10.1021/acs.inorgchem.5c03380
Inorg. Chem. 2025, 64, 21479−21488

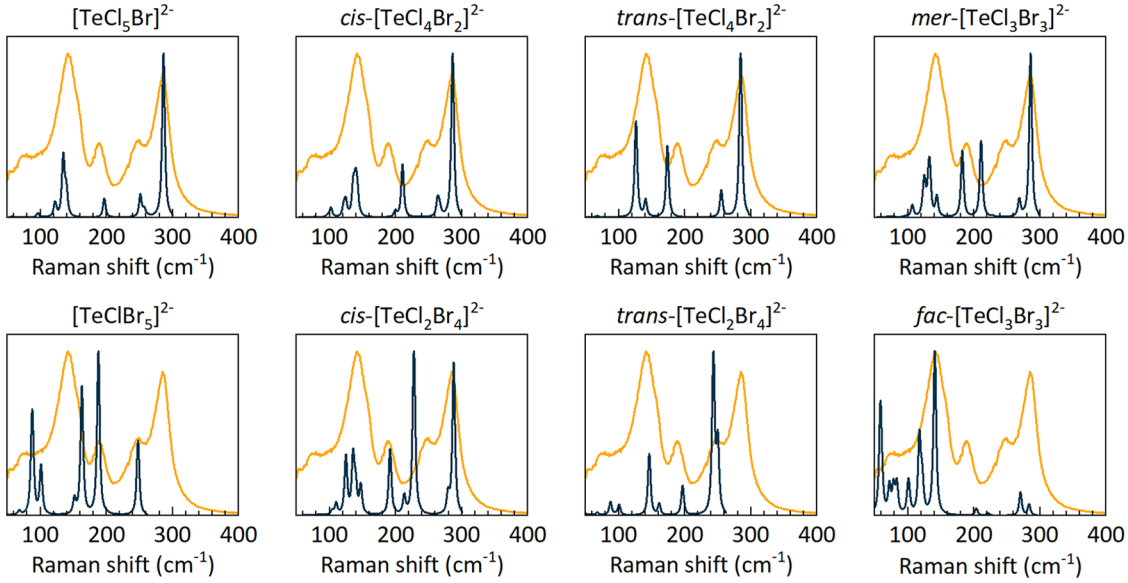

Figure 4. Comparison between the experimental Raman spectra (yellow) of high-Br $MA_2Te(Cl_{1-x}Br_x)_6$ and DFT-calculated spectra (blue) for different types of $[TeCl_{6-x}Br_x]^{2-}$ octahedra.

bond angle variance in the TeX_6 octahedron is 1.72 deg^2, which is less than that observed in MA_2TeCl_6(Figure 2(c)), where Te is symmetrically separated from the top and bottom Cl ions in a $[TeCl_6]^{2-}$ octahedron. The Cl atoms parallel to the *ab* plane have the same projected distances to the plane containing Te (1.417 Å) and bond angles (91.67°). All Te−Cl bond lengths are 2.547(3) Å at room temperature.

The projection distances along the *a*- and *c*-axes are summarized in Table 1. The distance between the $[TeX_6]^{2-}$ octahedra layers along the *c*-axis (**X(1)···X(2)**) is comparable to that of the pure MA_2TeCl_6 structure (**Cl···Cl**). Thus, the enlarged $[TeX_6]^{2-}$octahedra, due to Br-doping, are the main origin of the lattice expansion on *c*. On the other hand, the intra- and interoctahedra distances vary along the *a*-axis. Although the Te−X(1) bond length is lengthened by the addition of Br, the projected distances between halides along the *a*-axis may be identical to those in pure MA_2TeCl_6 due to the change in bond angles.

Crystal Structure of High-Br $MA_2Te(Cl_{1-x}Br_x)_6$. At higher Br concentrations, the high-Br $MA_2Te(Cl_{1-x}Br_x)_6$ at 295 K forms a rhombohedral structure $R\bar{3}m$, which is isostructural to other methylammonium hexachlorometallates.[21] $R\bar{3}m$ is a subgroup of $Fm\bar{3}m$, and is reached from the aristotype by in-phase rotation of all octahedra by approximate 5° around the cubic axes.[46] The cell volume is 342.7 Å^3/formula unit, and the pseudocubic lattice parameter is 11.178(1) Å. As illustrated in Figure 3(a), the $[TeX_6]^{2-}$ octahedron layer at z = 1/3 is separated from the layer at z = 0 by 2/3 and 1/3, respectively.

In the high-Br structure, no halide ordering is detectable, and all X positions have the same average Cl and Br occupancies. Refinement shows a 14.4% Br occupancy on the halide site, which matches well with the XPS compositional values (see Table S2). As a result, the bond lengths in $[TeX_6]^{2-}$ are identical at 2.581(1) Å. The bond angle variance of the octahedron is 0.53 deg^2. Figure 3(b) depicts the octahedra in the high-Br structure. Te is symmetrically separated between the halide layers with a projected distance of 1.471 Å. The $[TeBr_6]^{2-}$ octahedron in MA_2TeBr_6 (Figure 3(c)) has a longer Te−Br bond length (2.712(2) Å) with a nondistorted structure. All bond angles are 90°.

The projection distances of the high-Br $MA_2Te(Cl_{1-x}Br_x)_6$ lattice are summarized in Table 1. Although the octahedron is enlarged as the concentration of Br increases, the interoctahedral distances are shorter than those of MA_2TeCl_6. This is believed to be due to the different arrangements of the octahedral layers along the *c*-axis. However, the cation cavity is still expanded, which further increases the insertion of MA^+ into the $[TeX_6]^{2-}$ layers, which will be further discussed later.

Raman Spectroscopy. The discussion of the structure based on the SXD results indicates a partially ordered halide arrangement in the low-Br structure. As previous studies have shown a near-random halide distribution throughout the octahedra in mixed-halide compounds of the vacancy-ordered double perovskites,[35,47] the low-Br structure reported in this work appears unusual. Raman spectroscopy can be an effective local probe to understand the halide distribution in the compound. This is due to the presence of isolated octahedra in the double perovskites.

Following the work of Karim et al.,[35] DFT was used to simulate the Raman-active vibrational frequencies of Te octahedra with various Cl and Br octahedral coordinations. Since the Raman spectra of compounds with this structure type are dominated by the vibrational modes of the isolated $[BX_6]^{2-}$ octahedra, it is sufficient to calculate the Raman spectrum from each possible octahedron and compare it with the experimental data. Experimental Raman spectra were collected for comparison with the calculated spectra. This method was first validated using pure halide perovskites, MA_2TeCl_6 and MA_2TeBr_6. Figure S6 shows a good match between the experimental and calculated Raman spectra. The three Raman-active peaks correspond to the A_{1g}, E_g, and T_{2g} vibrations of a regular octahedron.

The possible local environments around Te in the mixed-halide compounds were then simulated by substituting an increasing number of Br ions on the 6 possible coordination sites in the primitive structure. Eight mixed-anion coordinations are possible (see Figure S7): $[TeCl_5Br]^{2-}$, *cis*-

https://doi.org/10.1021/acs.inorgchem.5c03380
Inorg. Chem. 2025, 64, 21479−21488

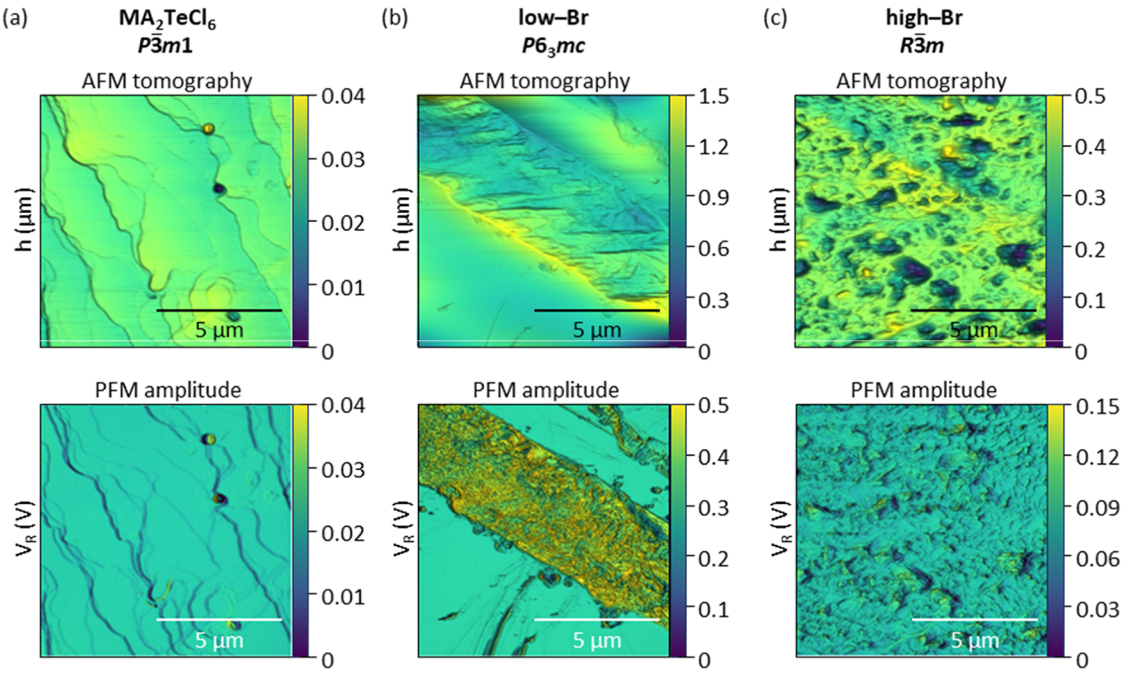

Figure 5. Topography and PFM signal on the (a) MA_2TeCl_6, (b) low- and (c) high-Br $MA_2Te(Cl_{1-x}Br_x)_6$ single-crystal surfaces over a 10 × 10 μm^2 area.

$[TeCl_4Br_2]^{2-}$, *trans*-$[TeCl_4Br_2]^{2-}$, *mer*-$[TeCl_3Br_3]^{2-}$, *fac*-$[TeCl_3Br_3]^{2-}$, *cis*-$[TeCl_2Br_4]^{2-}$, *trans*-$[TeCl_2Br_4]^{2-}$, and $[TeClBr_5]^{2-}$. The experimental Raman spectra for both low- and high-Br appear very similar, as shown in Figure S8, indicating that they have similar $[TeX_6]^{2-}$ coordination. In addition to the three peaks observed originating from $[TeCl_6]^{2-}$, there is an additional peak at *ca.* 190 cm^{-1} for both crystals, which has a higher intensity in the high-Br sample. Hence, it is reasonable to assume that both low-Br and high-Br samples contain the same type of $[TeX_6]^{2-}$, while the latter has a greater concentration of the octahedron responsible for the 190 cm^{-1} peak..

Figure 4 shows a comparison between the various DFT-calculated vibrational modes (in blue) and the high-Br experimental spectrum (in yellow). The best match to the experimental spectrum is observed with the calculated spectrum for $[TeCl_5Br]^{2-}$, and all others have a different number of vibrational modes and/or relative positions of the modes. Therefore, the Raman analysis suggests the homogeneity of octahedra that there is at most one Br atom within each $[TeX_6]^{2-}$ octahedron in both low- and high-Br structures.

SXD refinement places this Br ion in the X(1) plane, and the rest is occupied by Cl in the low-Br phase. If every octahedron contained exactly one Br ion, the Br anion content would be $\frac{1}{6}$ or 16.7%. In fact, the low-Br sample with ordered anions has only 6.8% Br from XPS, which would correspond to around 1 in 3 octahedra having a Br ion in the X(1) plane. The refined average occupancy of the X(1) site is 8.6% Br, which is close to 1 in 2 of the octahedra having a Br ion in the X(1) plane. The ordering observed in the low-Br compound may be dependent on the precise size of the octahedra relative to the A-site ion, which stabilizes the $P6_3mc$ structure.

Turning to the high-Br structure, which shows no anion ordering by SXD, the Raman also leads us to a similar conclusion that, aside from $[TeCl_6]^{2-}$, the only other octahedron present in significant amounts is $[TeCl_5Br]^{2-}$. However, the higher concentration of Br in the high-Br compound (10.1% from XPS, 14.4% from SXD refinement) indicates that more than half of the octahedra contain a Br ion in this compound. The reason for the lack of anion ordering in this composition is not clear; however, we can draw some conclusions from the solution-synthesized powder sample results. As shown in the SI, the nominal 6% Br sample contains 15.7% Br based on the XPS results, while its PXD pattern (Figure S1) primarily consists of a low-Br structure, with a minor component of a high-Br phase. The Raman spectra (Figure S9) matched well with the calculated spectrum for $[TeCl_5Br]^{2-}$. When the Br concentration further increases (>16.7%), a clear difference is observed in the Raman spectra. The peaks at *ca.* 73 and 156 cm^{-1} are consistent with the calculated spectrum for *fac*-$[TeCl_3Br_3]^{2-}$, and their increased intensity as well as the diminishing intensity above 200 cm^{-1} provide further evidence for the increased formation of *fac*-$[TeCl_3Br_3]^{2-}$. This does not imply that the octahedra in these compounds comprise solely $[TeCl_6]^{2-}$, $[TeCl_5Br]^{2-}$ and *fac*-$[TeCl_3Br_3]^{2-}$; rather, other components cannot be identified clearly.

Although the underlying cause of the polar ordering in the narrow composition range is not fully understood, we suggest some important factors. In the polar low-Br compound, the octahedra present are $[TeCl_6]^{2-}$ and $[TeCl_5Br]^{2-}$. The preference for $[TeCl_5Br]^{2-}$ over other mixed-anion octahedra is influenced by the overall halide composition. With the low-Br content making the presence of two or more Br ions in a single octahedron less likely, it is possible that this may also be driven by the greater stability of $[TeCl_5Br]^{2-}$. Thus, the preference for this specific octahedron may have an electronic basis. The second requirement for the polar phase is the arrangement of $[TeCl_5Br]^{2-}$ octahedra such that all Br ions fall in a common layer. This is likely driven by size effects, with the observed polar structure being an ordered arrangement available at this specific concentration of $[TeCl_5Br]^{2-}$.

https://doi.org/10.1021/acs.inorgchem.5c03380
Inorg. Chem. 2025, 64, 21479−21488

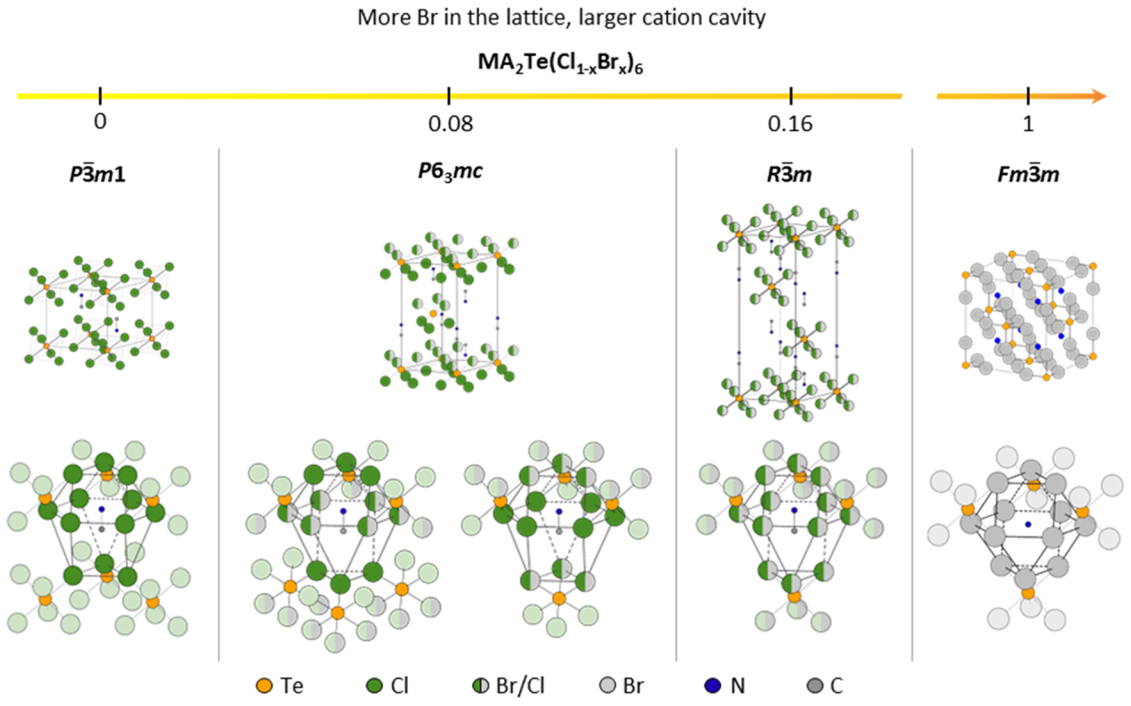

Figure 6. Schematic diagram of the unit cells (top) and MA cations located in the cavities (bottom) in MA_2TeCl_6, low-Br $MA_2Te(Cl_{1-x}Br_x)_6$, high-Br $MA_2Te(Cl_{1-x}Br_x)_6$, and MA_2TeBr_6 at room temperature. For the sake of clarity, the hydrogen atoms are not shown. The MA cation is replaced by one N atom in MA_2TeBr_6 to represent the spherical rotation of MA^+.

Increasing the concentration of $[TeCl_5Br]^{2-}$, as in the high-Br sample, or introducing other octahedra, such as in the solid-state synthesized compounds (as discussed in the SI), prevents the formation of an ordered polar structure. These collections of octahedra evidently do not order in the same way as the low-Br sample.

Partial anion ordering in low-Br $MA_2Te(Cl_{1-x}Br_x)_6$ leads to a polar structure that can exhibit piezoelectric properties. Materials that can be classified as piezoelectric are restricted to noncentrosymmetric point groups where the primitive unit cells possess a nonvanishing dipole moment. In the double perovskite, the interplay between the dynamics of the molecular ion (MA) and the inorganic octahedral cage leads to a noncentrosymmetric crystal structure.[48,49] $P6_3mc$ is a space group, which is known to be piezoelectric.[50−52] When external forces are applied, the unit cell experiences polarization and is able to sustain a dipole moment. An example is the double-perovskite K_2MnF_6 that crystallizes in both $Fm\bar{3}m$ (*c*) and $P6_3mc$ (*h*) space groups, but only presents piezoelectricity as h-K_2MnF_6, as it is symmetry-forbidden in its cubic phase.[51]

To attempt to measure the piezoelectric response, PFM was performed on the single-crystal surfaces, as illustrated in Figure 5. An AC electric field was applied to the sample while the AFM tip was maintained with a constant deflection over the sample. In response to the applied AC field, a piezoelectric material can expand or contract, resulting in a change in the deflection of the cantilever. Figure 5(a−c) shows the representative tomography of the crystal surface over a 10 × 10 μm^2 area, with the corresponding piezoresponse amplitude under an applied sample bias of 3 V shown below. Tomography shows light damage to the crystal surface, possibly due to the tweezers' handling. The piezoresponse is measured as a deflection error to detect the presence of lateral piezoelectric domains.

For the low-Br $MA_2Te(Cl_{1-x}Br_x)_6$ in Figure 5(b), a noticeable difference in the piezoresponse amplitude reveals the domain pattern. The presence of yellow and blue-green regions corresponds to low and high PFM amplitudes, respectively. The difference between the regions indicates the presence of specific polarization orientations within the compound: yellow is in-phase and the blue-green is out-of-phase to the incident electric field, which is beyond the scope of this work.[53,54] Meanwhile, the piezoresponse was absent for pure MA_2TeCl_6 (Figure 5(a)), while significantly lower and scattered for the high-Br phase (Figure 5(c)). These observations indicate that the presence of Br ions in the $[TeX_6]^{2-}$ octahedron does not automatically result in a piezoelectric structure. However, the Br/Cl ordering along the *c*-axis leads to a noncentrosymmetric crystal structure, which is essential to retain a dipole moment. The lattice distortions from the AC field result in polarization and observable piezoresponses.[55,56] Thus, the PFM results further support the presence of a noncentrosymmetric structure of low-Br $MA_2Te(Cl_{1-x}Br_x)_6$.

A-Site Cation Cavity. The A cation cavity undergoes alteration as the structure changes across the composition range studied. Although in each case the A-site cavity is still formed by 12 halide neighbors, its coordination changes with the different crystal structures, as depicted in Figure 6. We have previously determined that the MA^+ cation adopts a conical rotation in MA_2TeCl_6,[22] and we now carry out similar refinements of the average MA^+ position for the other structures reported here.

Uniquely for the compounds studied here, the low-Br structure with partial anion ordering has two distinct A-site environments: one of these (Figure 6(b), left) is similar to that found in MA_2TeCl_6, where MA^+ is coordinated to six $[TeX_6]^{2-}$ anions, with the bottom octahedra layer rotated by 180°. The other A-site environment (Figure 6(b), right) has a structure

https://doi.org/10.1021/acs.inorgchem.5c03380
Inorg. Chem. 2025, 64, 21479−21488

similar to that found in high-Br $MA_2Te(Cl_{1-x}Br_x)_6$ and MA_2TeBr_6, as shown in Figure 6(c,d), respectively, with the A-site surrounded by four $[TeX_6]^{2-}$ anions. In this way, the low-Br structure can be thought of as a mixture of the environments observed in MA_2TeCl_6 and MA_2TeBr_6.

Although the interlayer distance of the $[TeX_6]^{2-}$ octahedra (**X(1)**···**X(2)**) remains similar in the low-Br structure to that of MA_2TeCl_6, the A-site cavity itself is slightly larger due to the increased size of the octahedra. The MA^+ cations in the low-Br phase are 'inserted' more into the $[TeX_6]^{2-}$ layer, as indicated by the increased projected **N(1)**···**X(1)** and **N(2)**···**X(2)** distances in Table 1. The MA^+ cations surrounded by their cation cavities are illustrated in Figure S10. Both types of cavities in the low-Br structure contain, on average, 6 Cl and 6 Br ions; however, they have different halide coordinations. Therefore, although the heights of the two tetradecahedra and the hexagonal areas of their middle layers are almost the same, their volumes vary due to the difference in the length (i.e., **X(1)**···**X(1)** and **X(2)**···**X(2)**) of their top and bottom sides. The space near N(1) is smaller than that near N(2), which allows N(2) to insert deeper into the $[TeX_6]^{2-}$ layer, with a larger projected distance (**N**···**X**). Different halide coordinations also affect the molecular dynamics of MA^+. As illustrated by the ellipsoids in Figure S10(a), the N(1) spins have a more ellipsoidal shape, while N(2) is more spherical. This could explain the slightly increased C−N(2) bond length (1.359 Å) compared to C−N(1) (1.356 Å).

The MA^+ cation in high-Br $MA_2Te(Cl_{1-x}Br_x)_6$ is coordinated to four $[TeX_6]^{2-}$ octahedra, similar to the observed A-site cavity in MA_2SnCl_6.[57] The cavity size increases with additional Br (Figure S10(b)), resulting in further penetration of MA into the Te halide layers. The smaller distances between N and X may restrict the conical rotation of MA^+, hence increasing the projected C−N length on c to 1.394 Å, which is closer to the bond length in methylamine (1.469 Å).[58] As the Br concentration further increases to MA_2TeBr_6 (Figure 6(d)), the cavity shares a similar but now more symmetric tetradecahedron structure. The cavity space is sufficiently enlarged to allow for the spherical rotation of the MA molecule.

Overall, the MA^+ dynamics are closely related to the cavity size and shape. The rotation mode can be interpreted from the projected C−N bond length: MA^+ first experiences a more 'conical' rotation from MA_2TeCl_6 to low-Br structure, and then it is allowed to stay more vertically in the high-Br sample with a larger interlayer distance of $[TeX_6]^{2-}$ octahedra. Finally, with a much larger cavity, MA^+ rotates in a spherical manner in MA_2TeBr_6.

CONCLUSION

The counter-diffusion crystal growth technique is advantageous due to its ability to facilitate precise control over the halide ratio incorporated into the crystal lattice. Hence, low- and high-Br $MA_2Te(Cl_{1-x}Br_x)_6$ single crystals have been synthesized using the CDCG technique. Phase transitions are clearly observed by increasing the Br concentration in the $MA_2Te(Cl_{1-x}Br_x)_6$ ($0 \le x \le 1$) series at room temperature. The structure of low-Br $MA_2Te(Cl_{1-x}Br_x)_6$ is identified as $P6_3mc$, consistent with its piezoelectric response at room temperature, while the high-Br $MA_2Te(Cl_{1-x}Br_x)_6$ shares the same nonpiezoelectric crystal structure, $R\bar{3}m$, as MA_2SnCl_6. The structural evolution and molecular dynamics of $MA_2Te(Cl_{1-x}Br_x)_6$ were analyzed in detail. Uniquely, the halide distribution within the two mixed-halide compounds appears to be ordered with at most one bromine atom per $[TeX_6]^{2-}$ octahedron. This feature is distinct from the more common statistical or random mixing observed in many other mixed-halide perovskites.

ASSOCIATED CONTENT

Supporting Information

The Supporting Information is available free of charge at https://pubs.acs.org/doi/10.1021/acs.inorgchem.5c03380.

Additional results on solid state and solution phase syntheses, and Raman calculations (PDF)

Accession Codes

Deposition Numbers 2474594 and 2474805 contain the supplementary crystallographic data for this paper. These data can be obtained free of charge via the joint Cambridge Crystallographic Data Centre (CCDC) and Fachinformationszentrum Karlsruhe Access Structures service.

AUTHOR INFORMATION

Corresponding Author

Robert G. Palgrave − *Department of Chemistry, University College London, London WC1H 0AJ, U.K.;* orcid.org/0000-0003-4522-2486; Email: r.palgrave@ucl.ac.uk

Authors

Yuhan Liu − *Department of Chemistry, University College London, London WC1H 0AJ, U.K.; Department of Chemical Engineering, University College London, London WC1E 7JE, U.K.*

Prajna Bhatt − *Department of Chemistry, University College London, London WC1H 0AJ, U.K.; Istituto Officina dei Materiali (IOM)-CNR, Laboratorio TASC, Trieste I-34149, Italy*

Roxy Lee − *Department of Chemistry, University College London, London WC1H 0AJ, U.K.; Department of Energy Conversion and Storage, Danmarks Tekniske Universitet, 334 2800 Kgs. Lyngby, Denmark;* orcid.org/0000-0001-7845-0093

Avishek Dey − *Department of Chemistry, University College London, London WC1H 0AJ, U.K.; London Centre for Nanotechnology, University College London, London WC1H 0AH, U.K.*

Anna Regoutz − *Department of Chemistry, University College London, London WC1H 0AJ, U.K.; Department of Chemistry, University of Oxford, Inorganic Chemistry Laboratory, Oxford OX1 3QR, U.K.*

Robin S. Perry − *London Centre for Nanotechnology, University College London, London WC1H 0AH, U.K.; Department of Physics and Astronomy, University College London, London WC1E 6BT, U.K.*

Complete contact information is available at: https://pubs.acs.org/10.1021/acs.inorgchem.5c03380

Notes

The authors declare no competing financial interest.

ACKNOWLEDGMENTS

XPS was carried out at HarwellXPS, the National XPS Facility (EP/Y023587/1). Y.L. thanks the UCL-CSC scholarship scheme for PhD funding. The authors thank Dr. Jeremy Cockcroft for helpful discussions.

REFERENCES

(1) Suárez-Rodríguez, M.; de Juan, F.; Souza, I.; Gobbi, M.; Casanova, F.; Hueso, L. E. Nonlinear Transport in Non-Centrosymmetric Systems. *Nat. Mater.* **2025**, *24* (7), 1005−1018.

(2) Jakubas, R.; Rok, M.; Mencel, K.; Bator, G.; Piecha-Bisiorek, A. Correlation between Crystal Structures and Polar (Ferroelectric) Properties of Hybrids of Haloantimonates(Iii) and Halobismuthates-(Iii). *Inorg. Chem. Front.* **2020**, *7* (10), 2107−2128.

(3) Dang, Y.; Liu, X.; Cao, B.; Tao, X. Chiral Halide Perovskite crystals for Optoelectronic Applications. *Matter* **2021**, *4* (3), 794−820.

(4) Fabini, D. H.; Honasoge, K.; Cohen, A.; Bette, S.; McCall, K. M.; Stoumpos, C. C.; Klenner, S.; Zipkat, M.; Hoang, L. P.; Nuss, J.; Kremer, R. K.; Kanatzidis, M. G.; Yaffe, O.; Kaiser, S.; Lotsch, B. V. Noncollinear Electric Dipoles in a Polar Chiral Phase of $CsSnBr_3$ Perovskite. *J. Am. Chem. Soc.* **2024**, *146* (23), 15701−15717.

(5) Dang, Y.; Liu, X.; Cao, B.; Tao, X. Chiral Halide Perovskite Crystals for Optoelectronic Applications. *Matter* **2021**, *4* (3), 794−820.

(6) Kashikar, R.; Lisenkov, S.; Ponomareva, I. Coexistence of Polar and Antipolar Phases in Ferroelectric Halide Perovskite $CsGeBr_3$. *Phys. Rev. B* **2024**, *109* (2), No. L020101.

(7) Han, C.; Bradford, A. J.; McNulty, J. A.; Zhang, W.; Halasyamani, P. S.; Slawin, A. M. Z.; Morrison, F. D.; Lee, S. L.; Lightfoot, P. Polarity and Ferromagnetism in Two-Dimensional Hybrid Copper Perovskites with Chlorinated Aromatic Spacers. *Chem. Mater.* **2022**, *34* (5), 2458−2467.

(8) Charles, N.; Saballos, R. J.; Rondinelli, J. M. Structural Diversity from Anion Order in Heteroanionic Materials. *Chem. Mater.* **2018**, *30* (10), 3528−3537.

(9) Ovčar, J.; Leung, T. L.; Grisanti, L.; Skoko, Ž.; Vrankić, M.; Low, K.-H.; Wang, S.; You, P.-Y.; Ahn, H.; Lončarić, I.; Djurišić, A. B.; Popović, J. Mixed Halide Ordering as a Tool for the Stabilization of Ruddlesden−Popper Structures. *Chem. Mater.* **2022**, *34* (10), 4286−4297.

(10) Hodgkins, T. L.; Savory, C. N.; Bass, K. K.; Seckman, B. L.; Scanlon, D. O.; Djurovich, P. I.; Thompson, M. E.; Melot, B. C. Anionic Order and Band Gap Engineering in Vacancy Ordered Triple Perovskites. *Chem. Commun.* **2019**, *55* (21), 3164−3167.

(11) Maughan, A. E.; Ganose, A. M.; Scanlon, D. O.; Neilson, J. R. Perspectives and Design Principles of Vacancy-Ordered Double Perovskite Halide Semiconductors. *Chem. Mater.* **2019**, *31* (4), 1184−1195.

(12) Bhumla, P.; Jain, M.; Sheoran, S.; Bhattacharya, S. Vacancy-Ordered Double Perovskites Cs_2BI_6 (B = Pt, Pd, Te, Sn): An Emerging Class of Thermoelectric Materials. *J. Phys. Chem. Lett.* **2022**, *13* (50), 11655−11662.

(13) Faizan, M.; Bhamu, K. C.; Murtaza, G.; He, X.; Kulhari, N.; AL-Anazy, M. M.; Khan, S. H. Electronic and Optical Properties of Vacancy Ordered Double Perovskites A_2BX_6 (A = Rb, Cs; B = Sn, Pd, Pt; and X = Cl, Br, I): A First Principles Study. *Sci. Rep* **2021**, *11* (1), No. 6965.

(14) Ghorui, S.; Kangsabanik, J.; Aslam, M.; Alam, A. Optoelectronic and Transport Properties of Vacancy-Ordered Double-Perovskite Halides: A First-Principles Study. *Phys. Rev. Appl.* **2024**, *21* (2), No. 024036.

(15) Rahim, W.; Cheng, A.; Lyu, C.; Shi, T.; Wang, Z.; Scanlon, D. O.; Palgrave, R. G. Geometric Analysis and Formability of the Cubic A_2BX_6 Vacancy-Ordered Double Perovskite Structure. *Chem. Mater.* **2020**, *32* (22), 9573−9583.

(16) Brown, I. D. The Crystal Structure of K_2TeBr_6. *Can. J. Chem.* **1964**, *42* (12), 2758−2767.

(17) Caicedo-Dávila, S.; Cohen, A.; Motti, S. G.; Isobe, M.; McCall, K. M.; Grumet, M.; Kovalenko, M. V.; Yaffe, O.; Herz, L. M.; Fabini, D. H.; Egger, D. A. Disentangling the Effects of Structure and Lone-Pair Electrons in the Lattice Dynamics of Halide Perovskites. *Nat. Commun.* **2024**, *15* (1), No. 4184.

(18) Mozur, E. M.; Neilson, J. R. Cation Dynamics in Hybrid Halide Perovskites. *Annu. Rev. Mater. Res.* **2021**, *51* (1), 269−291.

(19) Lazarini, F. Caesium Enneabromodibismuthate(III). *Acta Crystallogr. B* **1977**, *33* (9), 2961−2964.

(20) Lee, J.-W.; Tan, S.; Seok, S. Il.; Yang, Y.; Park, N.-G. Rethinking the A Cation in Halide Perovskites. *Science* **2022**, *375* (6583), No. eabj1186, DOI: 10.1126/science.abj1186.

(21) Kume, Y.; Ikeda, R.; Nakamura, D. Structural Phase Transition in Various Methylammonium Hexahalometallates(IV) as Studied by the NQR of Halogens. *J. Magn. Reson.* **1979**, *33* (2), 331−344.

(22) Liu, Y.; Cockcroft, J. K.; Chen, Z.; Hayward, M. A.; Henry, P. F.; Perry, R. S.; Palgrave, R. G. Phase Transitions and Optical Properties of the Trigonal Perovskite $(CH_3NH_3)_2TeCl_6$. *J. Mater. Chem. C Mater.* **2022**, *10* (33), 11938−11945.

(23) Francisco-López, A.; Charles, B.; Alonso, M. I.; Garriga, M.; Campoy-Quiles, M.; Weller, M. T.; Goñi, A. R. Phase Diagram of Methylammonium/Formamidinium Lead Iodide Perovskite Solid Solutions from Temperature-Dependent Photoluminescence and Raman Spectroscopies. *J. Phys. Chem. C* **2020**, *124* (6), 3448−3458.

(24) Selivanov, N. I.; Murzin, A. O.; Yudin, V. I.; Kapitonov, Y. V.; Emeline, A. V. Counterdiffusion-in-Gel Growth of High Optical and Crystal Quality $MAPbX_3$ ($MA = CH_3NH_3^+$, $X = I^-$, Br^-) Lead-Halide Perovskite Single Crystals. *CrystEngComm* **2022**, *24* (16), 2976−2981.

(25) Suib, S. L.; Weller, P. F. Gel Growth of Single Crystals of Some Rubidium and Cesium Tin Halides. *J. Cryst. Growth* **1980**, *48* (1), 155−160.

(26) Kresse, G.; Furthmüller, J. Efficient Iterative Schemes for Ab Initio Total-Energy Calculations Using a Plane-Wave Basis Set. *Phys. Rev. B* **1996**, *54* (16), 11169−11186.

(27) Blöchl, P. E. Projector Augmented-Wave Method. *Phys. Rev. B* **1994**, *50* (24), 17953−17979.

(28) Kresse, G.; Joubert, D. From Ultrasoft Pseudopotentials to the Projector Augmented-Wave Method. *Phys. Rev. B* **1999**, *59* (3), 1758−1775.

(29) Perdew, J. P.; Burke, K.; Ernzerhof, M. Generalized Gradient Approximation Made Simple. *Phys. Rev. Lett.* **1996**, *77* (18), 3865−3868.

(30) Perdew, J. P.; Ruzsinszky, A.; Csonka, G. I.; Vydrov, O. A.; Scuseria, G. E.; Constantin, L. A.; Zhou, X.; Burke, K. Restoring the Density-Gradient Expansion for Exchange in Solids and Surfaces. *Phys. Rev. Lett.* **2008**, *100* (13), No. 136406.

(31) Pulay, P. Ab Initio Calculation of Force Constants and Equilibrium Geometries in Polyatomic Molecules. *Mol. Phys.* **1969**, *17* (2), 197−204.

(32) Porezag, D.; Pederson, M. R. Infrared Intensities and Raman-Scattering Activities within Density-Functional Theory. *Phys. Rev. B* **1996**, *54* (11), 7830−7836.

(33) Fonari, A.; Stauffer, S. *Vasp_raman.Py*, Github 2013.

(34) Jackson, A. J.; M Ganose, A.; Regoutz, A.; Egdell, R. G.; O Scanlon, D. Galore: Broadening and Weighting for Simulation of Photoelectron Spectroscopy. *J. Open Source Software* **2018**, *3* (26), No. 773.

(35) Karim, M. M. S.; Ganose, A. M.; Pieters, L.; Leung, W. W. W.; Wade, J.; Zhang, L.; Scanlon, D. O.; Palgrave, R. G. Anion Distribution, Structural Distortion, and Symmetry-Driven Optical Band Gap Bowing in Mixed Halide Cs_2SnX_6 Vacancy Ordered Double Perovskites. *Chem. Mater.* **2019**, *31* (22), 9430−9444.

(36) Agilent. *CrysAlisPRO*; Agilent Technologies Ltd: Yarnton, England, 2014.

(37) Sheldrick, G. M. Crystal Structure Refinement with SHELXL. *Acta Crystallogr. C Struct. Chem.* **2015**, *71* (Md), 3−8.

(38) Sheldrick, G. M. SHELXT - Integrated Space-Group and Crystal-Structure Determination. *Acta Crystallogr. A* **2015**, *71* (1), 3−8.

(39) Dolomanov, O. V.; Bourhis, L. J.; Gildea, R. J.; Howard, J. A. K.; Puschmann, H. OLEX2: A Complete Structure Solution, Refinement and Analysis Program. *J. Appl. Crystallogr.* **2009**, *42* (2), 339−341.

(40) MacRae, C. F.; Sovago, I.; Cottrell, S. J.; Galek, P. T. A.; McCabe, P.; Pidcock, E.; Platings, M.; Shields, G. P.; Stevens, J. S.;

https://doi.org/10.1021/acs.inorgchem.5c03380
Inorg. Chem. 2025, 64, 21479−21488

Towler, M.; Wood, P. A. Mercury 4.0: From Visualization to Analysis, Design and Prediction. *J. Appl. Crystallogr.* **2020**, *53* (1), 226−235.
(41) Momma, K.; Izumi, F. *VESTA 3* for Three-Dimensional Visualization of Crystal, Volumetric and Morphology Data. *J. Appl. Crystallogr.* **2011**, *44* (6), 1272−1276.
(42) Kume, Y.; Ikeda, R.; Nakamura, D. Phase Transitions of Methylammonium Hexahalotellurates(IV) as Revealed by the Nuclear Quadrupole Resonance of Halogens. *J. Phys. Chem. A* **1978**, *82* (17), 1926−1930.
(43) Evans, H. A.; Fabini, D. H.; Andrews, J. L.; Koerner, M.; Preefer, M. B.; Wu, G.; Wudl, F.; Cheetham, A. K.; Seshadri, R. Hydrogen Bonding Controls the Structural Evolution in Perovskite-Related Hybrid Platinum(IV) Iodides. *Inorg. Chem.* **2018**, *57* (16), 10375−10382.
(44) Ju, D.; Zheng, X.; Yin, J.; Qiu, Z.; Türedi, B.; Liu, X.; Dang, Y.; Cao, B.; Mohammed, O. F.; Bakr, O. M.; Tao, X. Tellurium-Based Double Perovskites A_2TeX_6 with Tunable Band Gap and Long Carrier Diffusion Length for Optoelectronic Applications. *ACS Energy Lett.* **2019**, *4* (1), 228−234.
(45) Shannon, R. D. Revised Effective Ionic Radii and Systematic Studies of Interatomic Distances in Halides and Chalcogenides. *Acta Crystallogr., Sect. A* **1976**, *32* (5), 751−767.
(46) Lufaso, M. W.; Barnes, P. W.; Woodward, P. M. Structure Prediction of Ordered and Disordered Multiple Octahedral Cation Perovskites Using *SPuDS*. *Acta Crystallogr. B* **2006**, *62* (3), 397−410.
(47) Yuan, G.; Huang, S.; Qin, S.; Wu, X.; Ding, H.; Lu, A. Structural, Optical, and Thermal Properties of $Cs_2SnI_{6-x}Br_x$ Mixed Perovskite Solid Solutions. *Eur. J. Inorg. Chem.* **2019**, *2019* (20), 2524−2529.
(48) Paul, T.; Sahoo, A.; Maiti, S.; Mandal, S.; Bhattacharjee, S.; Maity, A.; Chattopadhyay, K. K. Observation of Piezoelectricity in a Lead-Free $Cs_2AgBiBr_6$ Perovskite: A New Entrant in the Energy Harvesting Arena. *Nanoscale* **2024**, *16* (34), 16127−16139.
(49) Ashcroft, N. W.; Mermin, N. D. *Solid State Physics*; Crane, D. G., Ed.; Saunders College Publishing: Philadelphia, PA, USA, 1976.
(50) Yang, F. Physics of Ferroelectric Wurtzite $Al_{1-x}Sc_xN$ Thin Films. *Adv. Electron Mater.* **2025**, *11* (2), No. 2400279.
(51) Kasa, R.; Arai, Y.; Takahashi, T.; Adachi, S. Photoluminescent Properties of Cubic K_2MnF_6 Particles Synthesized in Metal Immersed HF/KMnO4 Solutions. *J. Appl. Phys.* **2010**, *108* (11), No. 113503.
(52) Yang, M.-M.; Zhu, T.-Y.; Renz, A. B.; Sun, H.-M.; Liu, S.; Gammon, P. M.; Alexe, M. Auxetic Piezoelectric Effect in Heterostructures. *Nat. Mater.* **2024**, *23* (1), 95−100.
(53) You, Y.-M.; Liao, W.-Q.; Zhao, D.; Ye, H.-Y.; Zhang, Y.; Zhou, Q.; Niu, X.; Wang, J.; Li, P.-F.; Fu, D.-W.; Wang, Z.; Gao, S.; Yang, K.; Liu, J.-M.; Li, J.; Yan, Y.; Xiong, R.-G. An Organic-Inorganic Perovskite Ferroelectric with Large Piezoelectric Response. *Science* **2017**, *357* (6348), 306−309.
(54) Veved, A.; Ejuh, G. W.; Djongyang, N. Review of Emerging Materials for PVDF-Based Energy Harvesting. *Energy Rep.* **2022**, *8*, 12853−12870.
(55) Kitahama, K.; Kiriyama, H.; Baba, Y. The Crystal Structures of Methylammonium Hexachlorostannate(IV) in the high- and Low-Temperature Phases Studied by X-Rays. *Bull. Chem. Soc. Jpn.* **1979**, *52* (2), 324−328.
(56) Allen, F. H.; Kennard, O.; Watson, D. G.; Brammer, L.; Orpen, A. G.; Taylor, R. Tables of Bond Lengths Determined by X-Ray and Neutron Diffraction. Part 1. Bond Lengths in organic Compounds. *J. Chem. Soc., Perkin Trans. 2* **1987**, No. 12, S1−S19.
(57) Kitahama, K.; Kiriyama, H.; Baba, Y. The Crystal structures of Methylammonium Hexachlorostannate(IV) in the High- and Low-Temperature Phases Studied by X-Rays. *Bull. Chem. Soc. Jpn.* **1979**, *52* (2), 324−328.
(58) Allen, F. H.; Kennard, O.; Watson, D. G.; Brammer, L.; Orpen, A. G.; Taylor, R. Tables of Bond Lengths Determined by X-Ray and Neutron Diffraction. Part 1. Bond Lengths in Organic compounds. *J. Chem. Soc., Perkin Trans. 2* **1987**, No. 12, S1−S19.

https://doi.org/10.1021/acs.inorgchem.5c03380
Inorg. Chem. 2025, 64, 21479−21488